VA-DEPTHNET: A VARIATIONAL APPROACH TO SINGLE IMAGE DEPTH PREDICTION

Anonymous authors
Paper under double-blind review

ABSTRACT

We introduce VA-DepthNet, a simple, effective, and accurate deep neural network approach for a single image depth prediction (SIDP) problem. The proposed approach advocate using classical first-order variational constraints for this problem. While state-of-the-art deep neural network methods for SIDP learn the scene depth from images in a supervised setting, they often overlook the invaluable invariances and priors in the rigid scene space, such as the regularity of the scene. The paper's main contribution is to reveal the benefit of classical and well-founded variational constraints in the neural network design for the SIDP task. It is shown that imposing first-order variational constraints in the scene space together with popular encoder-decoder-based network architecture design provides excellent results for the supervised SIDP task. The imposed first-order variational constraint makes the network aware of the depth gradient in the scene space, i.e., regularity[1]. The paper demonstrates the usefulness of the proposed approach via extensive evaluation and ablation analysis over several benchmark datasets, such as KITTI, NYU Depth V2, and SUN RGB-D. The VA-DepthNet at test time shows considerable improvements in depth prediction accuracy compared to the prior art and is accurate also at high-frequency regions in the scene space. At the time of submission, our method—labeled as VA-DepthNet, when tested on the KITTI official depth-prediction evaluation set, indexed second on the leader board, and our accuracy is top performing among the published method[2] [3].

1 INTRODUCTION

Over the last decade, neural networks have introduced a new prospect for the 3D computer vision field. It has led to significant progress on many long-standing problems in this field, such as multi-view stereo (Wang et al., 2021), vision-based simultaneous localization and mapping (Teed & Deng, 2021), novel view synthesis (Mildenhall et al., 2021) and others. Among several 3D vision problems, one of the challenging, if not impossible, to solve is the single image depth prediction (SIDP) problem. SIDP is indeed ill-posed—in a strict geometric sense, presenting an extraordinary challenge to reliably solving this inverse problem. Moreover, since we do not have access to multi-view images, it is hard to constrain this problem via well-proven geometric constraints (Hartley & Zisserman, 2003). Accordingly, this problem generally narrow-down to an ambitious fitting problem, and therefore, learning techniques provide a convenient way to predict an acceptable solution to this problem (Yuan et al., 2022; Yin et al., 2019).

Impressive earlier methods use Markov Random Field (MRF) to model monocular cues and the relation between several over-segmented image parts (Saxena et al., 2007; 2008). Nevertheless, with the recent surge in neural network architectures (Krizhevsky et al., 2012; Simonyan & Zisserman, 2014; He et al., 2016), which has an extraordinary capability to perform complex regression, many current works use deep learning to solve SIDP and have demonstrated high-quality results (Yuan et al., 2022; Aich et al., 2021; Bhat et al., 2021; Eigen et al., 2014; Fu et al., 2018; Lee et al., 2019; 2021). Popular recent methods for SIPD are, of course, supervised yet used less in real-world

[1]The term regularity is used loosely in a strict mathematical sense.

[2]http://www.cvlibs.net/datasets/kitti/eval_depth.php?benchmark=depth_prediction

[3]The code shall be public after the review.

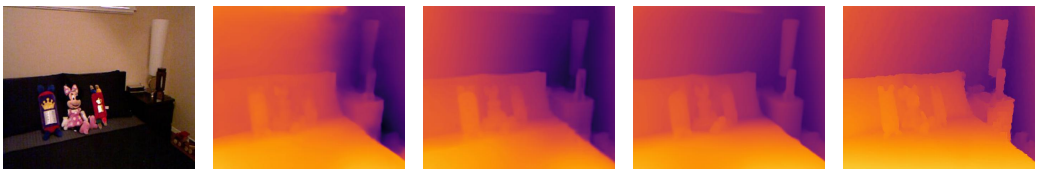

(a) Image (b) AdaBins (c) NeWCRFs (d) Ours (e) Ground Truth

Figure 1: Qualitative comparison of our method's depth result with recent state-of-the-art methods such as AdaBins (Bhat et al., 2021), NeWCRFs (Yuan et al., 2022) on NYU Depth V2 test set (Silberman et al., 2012). It can be inferred that our method provide high-quality depth prediction result and is closer to the ground truth.

applications as compared to popular geometric multiple view methods (Labbé & Michaud, 2019; Müller et al., 2022). Nonetheless, a good solution to SIDP is highly desirable in robotics (Tateno et al., 2017), virtual-reality (Hoiem et al., 2005), augmented reality (Du et al., 2020), view synthesis (Hoiem et al., 2005) and other related vision tasks (Liu et al., 2019).

In this paper, we advocate that despite the supervised approach being encouraging for the SIDP task, the restriction to study further and improve the nature of the solution must not wholly rely on the increase in the size and quality of the datasets. Instead, finding helpful geometric cues and scene priors that could help improve the SIDP results must be investigated. Not that scene priors have not been studied to improve SIDP accuracy in the past. For instance, Chen et al. (2016) uses pairwise ordinal relations between points to learn scene depth. On the contrary, Yin et al. (2019) uses surface normal as an auxiliary loss to improve the performance. Other heuristic approaches, such as Qi et al. (2018), jointly exploit the depth-to-normal relation for recovering scene depth and surface normal. Yet, such state-of-the-art SIDP methods have limitations; for example, Chen et al. (2016) ordinal relation for learning over-smooth the depth prediction results, thereby failing to preserve high-frequency surface details. Conversely, Yin et al. (2019) relies on good depth map prediction from a deep network and the idea of virtual normal, which is computed by randomly sampling three non-colinear points with large distances hence complex and heuristic in nature. As of Qi et al. (2018), it uses depth and normal consistency, which is good, yet it requires good depth map initialization. Further, depth is dependent on the structure information of the scene geometry. In contrast, surface normal is local and can be computed using small neighborhood relations. Thus, optimally exploiting joint normal and depth constraint effectiveness is challenging.

This brings us to the point that further generalization of the regression-based SIDP pipeline is required. As mentioned before, existing approaches in this direction have limitations and are complex. In this paper, we propose a simple approach that provides better depth accuracy and generalize well across the different scene (see Fig.1). To this end, we resort to the physics of variation (Mollenhoff et al., 2016; Oswald et al., 2012) in the neural network design for better generalization of the SIDP network, which by the way, keeps the essence of affine invariance (Yin et al., 2019). Our proposed network is trained in a fully-supervised manner while encouraging the network to be mindful of the scene regularity where the variation in the depth gradient is large (refer Sec.3.1). In simple terms, depth regression must be more than parameter fitting, and at some point, a mindful decision must be made—either by imaging features or by scene depth gradient variation, or both. As we demonstrate later in the paper, such an idea boosts the network's depth prediction overall accuracy while preserving the high-frequency and low-frequency scene details (see Fig.2).

Our introduced neural network for SIDP disentangles the absolute scale from the metric depth and models unscaled depth map as the optimal solution to the pixel-level variational constraints via weighted first-order difference respecting the neighboring pixel depth gradient. Compared to previous methods, the network task has been shifted away from pixel-wise metric depth learning to learning the first-order difference of the scene, which alleviates the scale ambiguity and favors scene regularity. To realize that, we first employ neural network to predict the first-order difference of the depth map. Then, we construct the partial differential equations representing the variational constraints by reorganizing the differences into a large matrix, i.e., an over-determined system of equations. Further, the network learns a weight matrix to eliminate redundant equations that does

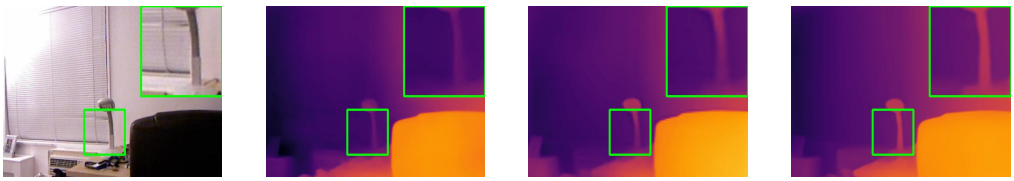

(a) Image (b) AdaBins (c) NeWCRFs (d) Ours

Figure 2: Qualitative comparison of our method's depth result with recent state-of-the-art methods such as AdaBins (Bhat et al., 2021), NeWCRFs (Yuan et al., 2022) on NYU Depth V2 test set (Silberman et al., 2012). It can be observed that our method predicts high-frequency details better than other recent methods.

not favor the introduced first-order difference constraint. Finally, the closed-form depth map solution is recovered via simple matrix operations.

When tested on the KITTI official (Geiger et al., 2012) and NYU Depth V2 (Silberman et al., 2012) test sets, our method supersedes prior art depth prediction accuracy by a large margin. Moreover, our pre-trained model on the NYU Depth V2 train set generalizes better on SUN RGB-D test set.

2 Prior Work

Predicting the scene's depth from a single image is a long-standing problem in computer vision, and impressive classical work exists to solve it. Nevertheless, in this work, we focus on a fully-supervised approach, and therefore, we discuss the related works that directly relate to the proposed approach. Broadly, we divide the popular supervised SIDP methods into three sub-categories.

***(i)* Depth Learning using Ranking or Ordinal Relation Constraint.** Zoran et al. (2015) and Chen et al. (2016) argue that the ordinal relation between points is easier to learn than the metric depth. To this end, Zoran et al. (2015) proposes constrained quadratic optimization while Chen et al. (2016) relies on the variation of the inception module to solve the problem. Later, Xian et al. (2020) propose structure-guided sampling strategies for point pairs to improve training efficiency. Recently, Lienen et al. (2021) elaborate on the use of listwise ranking method based on the Plackett-Luce model (Luce, 2012). The drawback of such approaches is that the ordinal relationship and ranking over smooth the depth solution making accurate metric depth recovery challenging.

***(ii)* Depth Learning using Surface Normal Constraint.** Hu et al. (2019) introduce normal loss in addition to the depth loss to overcome the distorted and blurry edges in the depth prediction. Yin et al. (2019) propose the concept of virtual normal to impose 3D scene constraint explicitly and capture the long-range relations in the depth prediction. The long-range dependency in 3D is introduced via random sampling of three non-colinear points at a large distance from the virtual plane. Lately, Long et al. (2021) proposed an adaptive strategy to compute the local patch surface normals at train time from a set of randomly sampled candidates and overlooks it during test time.

***(iii)* Depth Learning using other Heuristic Refinement Constraint.** There has been numerous works attempt to refine the depth prediction as a post-processing step. Liu et al. (2015), Li et al. (2015) and Yuan et al. (2022) propose various approaches to utilize the Conditional Random Fields (CRF) to smooth the depth map. Lee et al. (2019) and Patil et al. (2022) utilize the planar assumptions to regularize the predicted depth map. Qi et al. (2018) adopt an auxiliary network to predict the surface normal, and then refine the predicted depth map following their proposed heuristic rules. There are mainly two problems with such approaches: Firstly, these approaches rely on a good depth map initialization. Secondly, the heuristic rules and the assumptions might result in over-smoothed depth values at objects boundaries.

In this paper, we proffer the benefits of variational approach to overcome the limitations with the existing state-of-the-art methods. The proposed method can provide excellent depth prediction without impractical requirements such as good depth initialization, planar scene assumptions and others.

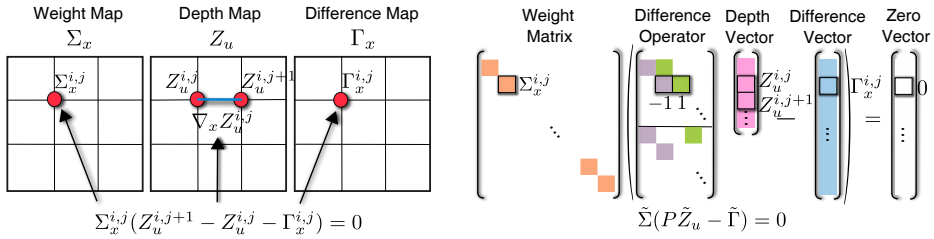

(a) First order depth variation along x-axis. (b) Overall matrix form by ordering all the terms.

Figure 3: **Illustration of the idea**. (a) Depth gradient constraint along x axis at location (i, j) in 4×4 matrix form. (b) Construction of the overall matrix formulation with constraints at all the pixel locations.

3 METHOD

In this section, we first describe our proposed variational constraint and then present the overall network architecture leading to the overall loss function.

3.1 VARIATIONAL CONSTRAINT

In this part, we introduce the variational constraint and how it can be useful for depth estimation. Consider the unscaled depth map as $Z_u \in \mathbb{R}^{H\times W}$, with (H, W) symbolizing the height and width, respectively. Assuming $\Gamma_x \in \mathbb{R}^{H\times W}$ and $\Gamma_y \in \mathbb{R}^{H\times W}$ as the gradient of Z_u in the x and y axis, we write

$$\nabla Z_u = [\Gamma_x,\ \Gamma_y]^{\mathrm{T}}. \tag{1}$$

Here, x and y subscript corresponds to the direction from left to right (x-axis) and top to bottom of the image (y-axis), respectively. Elaborating on this, we can write

$$\Gamma_x^{i,j} = \nabla_x Z_u^{i,j} = Z_u^{i,j+1} - Z_u^{i,j};\ \ \Gamma_y^{i,j} = \nabla_y Z_u^{i,j} = Z_u^{i+1,j} - Z_u^{i,j}. \tag{2}$$

Suppose we augment Eq.(2) expression for all (i, j), $i \in \{1, ..., H\}$ and $j \in \{1, ..., W\}$. In that case, we will end up with an over-determined system with $2HW$ equations in total. Given the predicted Γ_x and Γ_y, we aim to recover the HW unknown variables in Z_u. However, some of the equations could be spurious and deteriorate the overall depth estimation result rather than improving it. As a result, we must be mindful about selecting the equation that respects the imposed first-order constraint and maintains the depth gradient to have a meaningful fitting for better generalization. To that end, we introduce confidence weight $\Sigma_x \in [0, 1]^{H\times W}$, $\Sigma_y \in [0, 1]^{H\times W}$ for gradient along x, y direction. Consequently, we multiply the above two equations by the confidence weight term $\Sigma_x^{i,j}$ and $\Sigma_y^{i,j}$, respectively. On one hand, if the confidence is close to 1, the equation will have priority to be satisfied by the optimal Z_u. On the other hand, if the confidence is close to 0, we must ignore the equation. For better understanding, we illustrate the first order difference and weighted matrix construction in Fig.3 (a) and Fig.3(b).

Next, we reshape the Σ_x, Σ_y, Γ_x, Γ_y, and Z_u into column vectors $\tilde{\Sigma}_x \in [0, 1]^{HW\times 1}$, $\tilde{\Sigma}_y \in [0, 1]^{HW\times 1}$, $\tilde{\Gamma}_x \in \mathbb{R}^{HW\times 1}$, $\tilde{\Gamma}_y \in \mathbb{R}^{HW\times 1}$, and $\tilde{Z}_u \in \mathbb{R}^{HW\times 1}$, respectively. Organizing $\tilde{\Sigma} = \mathbf{diag}([\tilde{\Sigma}_x; \tilde{\Sigma}_y]) \in \mathbb{R}^{2HW\times 2HW}$ and $\tilde{\Gamma} = \mathbf{concat}[\tilde{\Gamma}_x; \tilde{\Gamma}_y] \in \mathbb{R}^{2HW\times 1}$, we can write the overall expression in a compact matrix form using simple algebra as follows

$$\tilde{\Sigma} P \tilde{Z}_u = \tilde{\Sigma}\tilde{\Gamma} \tag{3}$$

where $P \in \{1, -1\}^{2HW\times HW}$ is the first-order difference operator. Specifically, P is a sparse matrix with only a few elements as 1 or -1. The ith row of P provides the first-order difference operator for the ith equation. The position of 1 and -1 indicates which pair of neighbors to be considered for the constraint. Fig.3 (b) provides a visual intuition about this matrix equation.

Eq.(3) can be utilized to recover Z_u from the predicted Γ_x, Γ_y, Σ_x, and Σ_y. As alluded to above, we have more equations than unknowns, hence, we resort to recovering the optimal depth map

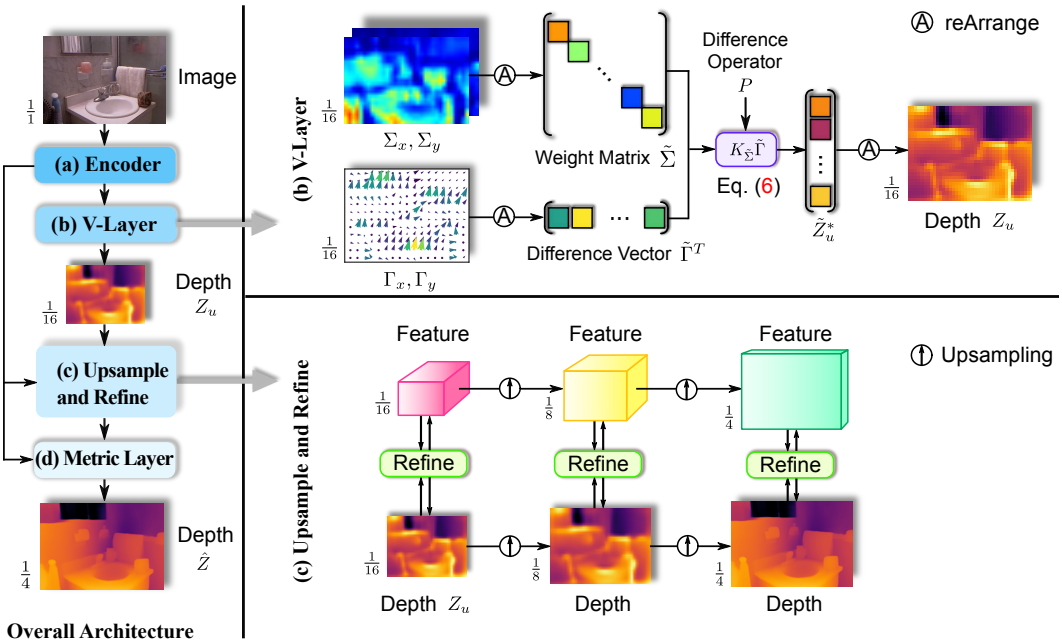

Figure 4: **Overview of our framework.** Given an input image, first an encoder is employed to extract features. Then we predict the depth map by the V-layer. Next, we gradually up-sample and refine the depth map. In the end, we recover the metric depth by the metric layer.

$\tilde{Z}_u^* \in \mathbb{R}^{HW\times 1}$ by minimizing the following equation:

$$\tilde{Z}_u^* = \underset{\tilde{Z}_u}{\arg\min}\, ||\tilde{\Sigma}(P\tilde{Z}_u - \tilde{\Gamma})||_2. \tag{4}$$

Refer Appendix for the full derivation. The closed-form solution can be written as follows:

$$\tilde{Z}_u^* = \overbrace{(P^T\tilde{\Sigma}^2 P)^{-1}P^T\tilde{\Sigma}^2}^{K_{\tilde{\Sigma}}}\tilde{\Gamma}. \tag{5}$$

Denote $K_{\tilde{\Sigma}} \triangleq (P^T\tilde{\Sigma}^2 P)^{-1}P^T\tilde{\Sigma}^2$ in Eq.(5), we write overall equation as $\tilde{Z}_u^* = K_{\tilde{\Sigma}}\tilde{\Gamma}$. Next, we describe the overall network architecture.

3.2 Overall Network Architecture

Our overall network architecture is composed of four main modules as follows.

***(a)* Encoder.** Given an input image, the encoder computes the hierarchical feature maps through a series of stages. To be precise, our encoder has four stages. Each stage contains transformer blocks (Liu et al., 2021b). At the end of each stage, we collect the final feature map as the output of the encoder resulting in the encoded feature maps with strides 4, 8, 16, and 32, respectively. Our encoder module is inspired by Liu et al. (2021b), a recent state-of-the-art transformer network design. We used it as our backbone by removing the final global pooling layer and fully connected layer.

***(b)* Variational Layer (V-Layer).** The goal of this layer is to compute a map from encoded feature map to unscaled depth map, which adheres to the first order variational constraint. As of V-layer, we feed the feature maps of strides 16 and 32 as input which is the output of the encoder. Since these features are at different resolution, we up-sample the feature map of stride 32 to stride 16 via bi-linear interpolation and concatenate to construct $I_\Phi \in \mathbb{R}^{C\times H\times W}$, where (H, W, C) symbolizing the height, width, and the number of channels, respectively. Note that H, W is not the same as the original resolution of the ground-truth depth and images. We use of two convolutional layers on I_Φ to predict the depth gradient and corresponding weight for each pixel as follows:

$$\{\Gamma_x, \Gamma_y, \Sigma_x, \Sigma_y\} = f(I_\Phi; \theta) \tag{6}$$

where, $f(I_\Phi;\theta)$ denotes the convolutional layers with parameters θ. The predicted depth gradients Γ_x and Γ_y are observed to be more accurate at smooth surface than at boundaries. This brings us again to the point made above that we must take care of which first order constraint must be included and discarded during regression. Using the Eq.(6) prediction, we construct the variational constraint Eq.(3), and obtain the unscaled depth map following Eq.(5). The resulting depth map has a resolution of 1/16 to the original image, which is later upsampled to the appropriate dimension.

To capture more scene features, we generate multiple channels (denoted as S) of $\{\Gamma_x, \Gamma_y, \Sigma_x, \Sigma_y\}$ using Eq.(6). As a result, we have a group of depth maps stacked along the channel dimension. For a feature map with spatial resolution $H \times W$, our V-layer has a complexity of $O(H^3W^3)$. To overcome complexity issue, we perform V-layer operation on feature maps with stride 16 and then up-sample and refine the depth maps in the later stage. The V-layer pipeline is shown in Fig.4(b).

(c) **Upsample and Refine.** This module upsamples and refines the input depth map via encoded features at a given depth map resolution. To this end, we perform refinement at three different resolutions in a hierarchical manner. Given the V-layer depth map at 1/16 resolution, we first refine the depth via encoded features at this resolution. Concretely, this refinement is done using the following set of operations. (1) concatenate the feature map and the depth map; (2) use one convolutional layer with ReLU activation to fuse the feature and depth information; and (3) predict refined feature and depth map via a convolutional layer. Later, the refined features and depth map is upsampled and fed into 1/8 for later refinement using the same above set of operations. Finally, the exact is done at 1/4 resolution. Note that these steps are performed in a sequel. At the end of this module, we have a depth map of 1/4 of the actual resolution. The upsample and refine procedure is shown in Fig.4(c).

(d) **Metric Layer.** We must infer the global scene scale and shift to recover the metric depth. For this, we perform global max pooling on the encoded feature map of stride 32. The resulting vector is fed into a stack of fully connected layers to regress the two scalars, i.e., one representing the scale and while other representing the shift. Using the feature map of stride 32 is motivated by the observation that we have a much richer global scene context using it than at higher depth resolution. It also provides a good compromise between computational complexity and accuracy.

3.3 Loss Function

Depth Loss. It estimates the scale-invariant difference between the ground-truth depth and prediction at train time (Eigen et al., 2014). The difference is computed by upsampling the predicted depth map to the same resolution as the ground truth via bi-linear interpolation. Denoting the predicted and ground-truth depth as $\hat{Z} \in \mathbb{R}^{m\times n}$, $Z_{gt} \in \mathbb{R}^{m\times n}$ we compute the depth loss as follows

$$\mathcal{L}_{depth}(\hat{Z}, Z_{gt}) = \frac{1}{N}\sum_{(i,j)}(e^{i,j})^2 - \frac{\alpha}{N^2}(\sum_{i,j} e^{i,j})^2, \text{ where, } e^{i,j} = \log \hat{Z}^{i,j} - \log Z_{gt}^{i,j}. \quad (7)$$

Here, N is the number of positions with valid measurements and $\alpha \in [0, 1]$ is a hyper-parameter. Note that the above loss is used for valid measurements only.

Variational Loss. We define this loss using the output of V-layer. Suppose the ground-truth depth map to be $Z_{gt} \in \mathbb{R}^{m\times n}$ and the predicted depth map for S channel as $Z_u \in \mathbb{R}^{S\times H\times W}$. Since the depth resolution is not same at this layer, we down-sample the ground-truth. It is observed via empirical study that low-resolution depth map in fact help capture the first-order variational loss among distant neighbors. Accordingly, we down sample the Z_{gt} instead of upsamping Z_u. We down-sampled Z_{gt} denoted as $Q_{gt} \in \mathbb{R}^{H\times W}$ by random pooling operation, i.e., we randomly select a location where we have a valid measurement since ground-truth data may have pixels with no depth values. The coordinates of selected location in $Z_{gt} \mapsto Z_u \in \mathbb{R}^{S\times H\times W}$ and the corresponding depth value is put in $\hat{Q} \in \mathbb{R}^{S\times H\times W}$ via bi-linear interpolation. We compute the variational loss as

$$\mathcal{L}_{var}(\hat{Q}, Q_{gt}) = \frac{1}{N'}\sum_{(i,j)} |\text{Conv}(\hat{Q})^{i,j} - \nabla Q_{gt}^{i,j}| \quad (8)$$

where N' is the number of positions having valid measurements, ∇ symbolises the first-order difference operator, and Conv refers to the convolutional layer.

Total Loss. We define the total loss as the sum of the depth loss and the variational loss i.e., $\mathcal{L} = \mathcal{L}_{depth} + \lambda\mathcal{L}_{var}$, where λ is the regularization parameter set to 0.1 for all our experiments.

Table 1: Comparison against the state-of-the-art methods on the NYU test set (Silberman et al., 2012). Methods with † utilize more training images. Please refer to Sec.4.1 for details.

Method	SILog ↓	Abs Rel ↓	RMS↓	RMS log↓	δ_1 ↑	δ_2 ↑
GeoNet† (Qi et al., 2018)	-	0.128	0.569	-	0.834	0.960
DORN† (Fu et al., 2018)	-	0.115	0.509	-	0.828	0.965
VNL† (Yin et al., 2019)	-	0.108	0.416	-	0.875	0.976
TransDepth (Yang et al., 2021)	-	0.106	0.365	-	0.900	0.983
ASN† (Long et al., 2021)	-	0.101	0.377	-	0.890	0.982
BTS (Lee et al., 2019)	11.533	0.110	0.392	0.142	0.885	0.978
DPT-Hybird† (Ranftl et al., 2021)	-	0.110	0.357	-	0.904	0.988
AdaBins† (Bhat et al., 2021)	10.570	0.103	0.364	0.131	0.903	0.983
ASTrans (Chang et al., 2021)	10.429	0.103	0.374	0.132	0.902	0.985
NeWCRFs (Yuan et al., 2022)	9.102	0.095	0.331	0.119	0.922	**0.992**
Ours	**8.198**	**0.086**	**0.304**	**0.108**	**0.937**	**0.992**
% Improvement	-9.93%	-9.47%	-8.16%	-9.24%	+1.63%	+0.00%

Table 2: Comparison against the state-of-the-art methods on the the KITTI official test set (Geiger et al., 2012). We only list the results from the published methods. Please refer to Sec.4.1 for details.

Method	SILog↓	Abs Rel↓	Sq Rel↓	iRMS↓
DLE (Liu et al., 2021a)	11.81	9.09	2.22	12.49
DORN (Fu et al., 2018)	11.80	8.93	2.19	13.22
BTS (Lee et al., 2019)	11.67	9.04	2.21	12.23
BANet (Aich et al., 2021)	11.55	9.34	2.31	12.17
PWA (Lee et al., 2021)	11.45	9.05	2.30	12.32
ViP-DeepLab (Qiao et al., 2021)	10.80	8.94	2.19	11.77
NeWCRFs (Yuan et al., 2022)	10.39	8.37	1.83	11.03
Ours	**9.84**	**7.96**	**1.66**	**10.44**
% Improvement	-5.29%	-4.90%	-9.29%	-5.35%

4 Experiments and Results

Implementation Details We implemented our method in PyTorch 1.7.1 (Python 3.8) with CUDA 11.0. The software is simulated and evaluated on a computing machine with Quadro-RTX-6000 GPU (24GB Memory).

Datasets. We evaluated our approach on three popular benchmark dataset namely NYU Depth V2 (Silberman et al., 2012), KITTI (Geiger et al., 2012), and SUN RGB-D (Song et al., 2015). ***(a)*** **NYU Depth V2** contains images with 480×640 resolution with depth values ranging from 0 to 10 meters. We follow the train and test set split from Lee et al. (2019), which contains 24,231 train images and 654 test images. ***(b)*** **KITTI** contains images with 352×1216 resolution where depth values ranges 0 to 80 meters. The official split provides 42,949 training, 1,000 validation, and 500 test images. Eigen et al. (2014) provide another train and test set split for this dataset which has 23,488 training and 697 test images. ***(c)*** **SUN RGB-D** We preprocess its images to 480×640 resolution for consistency. The depth values ranges from 0 to 10 meters. We use the official test set (5050 images) for evaluation.

Training Details. We use (Liu et al., 2021b) network as our backbone, which is pre-trained on ImageNet (Deng et al., 2009). We use the Adam optimizer (Kingma & Ba, 2014) without weight decay. We decrease the learning rate from $3e^{-5}$ to $1e^{-5}$ by the cosine annealing scheduler. To avoid over-fitting, we augment the images by horizontal flipping. For KITTI (Geiger et al., 2012), the model is trained for 10 epochs for the official split and 20 epochs for the Eigen split (Eigen et al., 2014). For NYU Depth V2 (Silberman et al., 2012), the model is trained for 20 epochs.

Evaluation Metrics. We report statistical results on popular evaluation metrics such as square root of the Scale Invariant Logarithmic error (**SILog**), Relative Squared error (**Sq Rel**), Relative Absolute Error (**Abs Rel**), Root Mean Squared error (**RMS**), and threshold accuracy. Mathematical definition related to each one of them is provided in the Appendix.

4.1 Comparison to the State-of-the-Art

Tab.(1), Tab.(2), Tab.(3), and Tab.(4) provide statistical comparison results with the competing methods on NYU Depth V2, KITTI official split, KITTI Eigen split, and SUN RGB-D, respectively. Our

Table 3: Comparison with the state-of-the-art methods on the KITTI Eigen test set (Eigen et al., 2014).

Method	SILog ↓	Abs Rel ↓	RMS↓	RMS log↓	δ_1 ↑	δ_2 ↑
DORN (Fu et al., 2018)	-	0.072	0.273	0.120	0.932	0.984
VNL (Yin et al., 2019)	-	0.072	0.326	0.117	0.938	0.990
TransDepth (Yang et al., 2021)	8.930	0.064	0.275	0.098	0.956	0.994
BTS (Lee et al., 2019)	8.933	0.060	0.280	0.096	0.955	0.993
DPT-Hybird (Ranftl et al., 2021)	-	0.062	0.257	-	0.959	0.995
AdaBins (Bhat et al., 2021)	8.022	0.058	0.236	0.089	0.964	0.995
ASTrans (Chang et al., 2021)	7.897	0.058	0.269	0.089	0.963	0.995
NeWCRFs (Yuan et al., 2022)	6.986	0.052	0.213	0.079	0.974	**0.997**
Ours	**6.817**	**0.050**	**0.209**	**0.076**	**0.977**	**0.997**
% Improvement	-2.42%	-3.85%	-1.88%	-3.80%	+0.03%	+0.00%

Table 4: Comparison with AdaBins and NeWCRFs on SUN RGB-D test set. All methods are trained on NYU Depth V2 train set without fine-tuning on SUN RGB-D.

Method	SILog ↓	Abs Rel ↓	RMS↓	RMS log↓	δ_1 ↑	δ_2 ↑
AdaBins(Bhat et al., 2021)	13.652	0.110	0.321	0.137	0.906	0.982
NeWCRFs (Yuan et al., 2022)	13.695	0.105	0.322	0.138	0.920	0.980
Ours	**12.596**	**0.094**	**0.299**	**0.127**	**0.929**	**0.983**
% Improvement	-7.73%	-10.48%	-6.85%	-7.30%	+0.98%	+0.10%

proposed approach shows the best results for all the evaluation metrics. Particularly on the NYU test set, we reduce the SILog error from the previous best result, 9.102 to 8.439, and increase δ_1 from 0.922 to 0.937. Visualization of predicted depth maps and intermediate results in V-layer are presented in the Appendix.

For the SUN RGB-D test set, all competing models, including ours, are trained on the NYU Depth V2 training set (Silberman et al., 2012) *without* fine-tuning on the SUN RGB-D. In addition, we align the predictions from all the models with the ground truth by a scale and shift following Ranftl et al. (2020). Tab.(4) results show our method's better generalization capability than other approaches. Extensive visual results are provided in the Appendix and supplementary video.

4.2 Ablation Study

All the ablation presented below is conducted on NYU Depth V2 test set (Silberman et al., 2012).

***(i)* Effect of V-Layer.** To understand the benefit and outcome of our introduced variational layer compared to other popular alternative layers in deep-neural networks for this problem, we performed this ablation study. We replace our V-layer firstly with a convolutional layer and later with a self-attention layer. Tab.(5) provides the depth prediction accuracy for this ablation. For each introduced layer in Tab.(5), the first and second rows show the performance of the depth map predicted *with* (w) and *without* (w/o) subsequent refinements (refer Sec.3.2(c)), respectively. For the self-attention layer, we follow the ViT (Dosovitskiy et al., 2020) and set the patch size to be one as we use the feature map with stride 16. We also adopt the learnable position embedding (PE) with 128-dimension. We set the number of heads to be 4 and the number of hidden units to be 512. As shown in Tab.(5), our V-layer indeed help improve the accuracy of depth prediction compared to other well-known layers. More experiments on KITTI and SUN RBG-D are provided in the Appendix.

***(ii)* Performance with Different Network Backbone.** We evaluate the effects of our V-layer with different types of network backbones. For this ablation, we use Swin-Large (Liu et al., 2021b),

Table 5: **Benefit of V-layer.** We replace the proposed V-layer with a single convolutional layer and a self-attention layer, and evaluate the accuracy of depth map predicted with and without subsequent refinements.

Layer	Refine	SILog ↓	Abs Rel ↓	RMS↓	RMS log ↓	δ_1 ↑	δ_2 ↑
Convolution	w/o	8.830	0.090	0.325	0.114	0.927	0.990
	w/	8.688	0.089	0.317	0.113	0.928	0.991
Self-Attention + PE	w/o	8.790	0.090	0.318	0.114	0.927	0.990
	w/	8.595	0.089	0.316	0.112	0.929	0.991
V-Layer	w/o	8.422	0.087	0.308	0.110	0.936	0.990
	w/	**8.198**	**0.086**	**0.304**	**0.108**	**0.937**	**0.992**

Swin-Small (Liu et al., 2021b), and ConvNeXt-Small (Liu et al., 2022). The SILog error is shown in Fig.5. The results show that our V-layer improves the transformer and the convolutional network performance. An important observation is that our V-layer shows excellent improvements in depth prediction accuracy on weaker network backbones.

***(iii)* Performance with change in the value of S.** For this ablation, we change the value of S in the V-layer and observed its effects (refer Sec.3.2). By increasing S, we generate more channels of $\tilde{\Gamma}$ and $\tilde{\Sigma}$ which in-effect increases V-layer parameters. In the subsequent step, we expand the number of channels to 128 by a convolutional layer to use the subsequent layer as it is. The results are shown in Tab.(6). For reference, we also present the result by replacing the V-layer with a convolutional layer in the first row in Tab.(6). By increasing the number of channels, we can reduce the SILog error, at the price of the speed (FPS). Yet, no real benefit is observed with S more than 16.

***(iv)* Effect of Confidence weight matrix & Difference Operator in V-Layer.** For this ablation, we study the our network's depth prediction under four different settings. (a) without V-layer and replace it with convolutional layer (b) without the confidence weight matrix (c) with learnable difference operator and (d) our full model. The depth prediction accuracy observed under these settings is provided in Tab.(7). Clearly, our full model has better accuracy. An important empirical observation, we made during this test is when we keep P learnable V-layer has more learnable parameters, the performance becomes worse than with fixed difference operator.

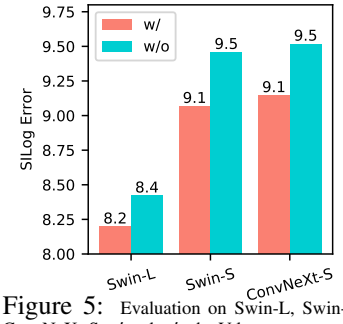

Figure 5: Evaluation on Swin-L, Swin-S, ConvNeXt-S **w/** and **w/o** the V-layer.

Table 6: Analysis of the number of feature groups. More groups reduce the SILog error.

	SILog↓	Abs Rel↓	RMS↓	FPS ↑
w/o V-layer	8.688	0.089	0.317	**9.343**
1	8.456	0.088	0.310	8.175
16	8.198	0.086	**0.304**	7.032
128	**8.172**	**0.085**	0.309	3.320

Table 7: Analysis of the confidence weight matrix $\tilde{\Sigma}$ and the difference operator P.

	SILog↓	Abs Rel↓	RMS ↓
(a) w/o V-layer	8.688	0.089	0.317
(b) w/o $\tilde{\Sigma}$	8.537	0.089	0.316
(c) learnable P	8.355	0.088	0.310
(d) **full**	**8.198**	**0.086**	**0.304**

4.3 Network Processing Time & Parameters

We compared our method's inference time and the number of model parameters to the AdaBins (Bhat et al., 2021) and the NeWCRFs (Yuan et al., 2022). The inference time is measured on the NYU Depth V2 test set with batch size 1. We have removed the ensemble tricks in AdaBins and NeWCRFs. As is shown in Tab.(8), our method is faster and better than AdaBins and NeWCRFs using Swin-Small backbone. With the same backbone as the NeWCRFs, i.e. Swin-Large, we achieve much better depth prediction results. Hence, our method with Swin-Small backbone provides a better balance between accuracy, speed and memory foot-print.

Table 8: Comparison of the inference time and parameters against AdaBins and NeWCRFs on NYU Depth V2. We show our results using the Swin-Small and Swin-Large backbone.

	AdaBins (Bhat et al., 2021)	NeWCRFs (Yuan et al., 2022)	Ours (Small)	Ours (Large)
SILog Error ↓	10.651	9.171	**9.069**	**8.198**
Speed (FPS) ↑	5.638	10.551	**11.891**	7.032
Param (M) ↓	**75**	258	**76**	249

5 Conclusion

In conclusion, a simple and effective approach for inferring scene depth from a single image is introduced. The proposed SIDP approach is shown to better exploit the rigid scene prior, which is generally overlooked by the existing neural network-based methods. Our approach does not make explicit assumptions about the scene other than the scene gradient regularity, which holds for typical indoor or outdoor scenes. When tested on popular benchmark datasets, our method shows significantly better results than the prior art, both qualitatively and quantitatively.

REFERENCES

Shubhra Aich, Jean Marie Uwabeza Vianney, Md Amirul Islam, and Mannat Kaur Bingbing Liu. Bidirectional attention network for monocular depth estimation. In *2021 IEEE International Conference on Robotics and Automation (ICRA)*, pp. 11746–11752. IEEE, 2021.

Shariq Farooq Bhat, Ibraheem Alhashim, and Peter Wonka. Adabins: Depth estimation using adaptive bins. In *Proceedings of the IEEE/CVF Conference on Computer Vision and Pattern Recognition*, pp. 4009–4018, 2021.

Wenjie Chang, Yueyi Zhang, and Zhiwei Xiong. Transformer-based monocular depth estimation with attention supervision. In *32nd British Machine Vision Conference (BMVC 2021)*, 2021.

Weifeng Chen, Zhao Fu, Dawei Yang, and Jia Deng. Single-image depth perception in the wild. *Advances in neural information processing systems*, 29, 2016.

Jia Deng, Wei Dong, Richard Socher, Li-Jia Li, Kai Li, and Li Fei-Fei. Imagenet: A large-scale hierarchical image database. In *2009 IEEE conference on computer vision and pattern recognition*, pp. 248–255. Ieee, 2009.

Alexey Dosovitskiy, Lucas Beyer, Alexander Kolesnikov, Dirk Weissenborn, Xiaohua Zhai, Thomas Unterthiner, Mostafa Dehghani, Matthias Minderer, Georg Heigold, Sylvain Gelly, et al. An image is worth 16x16 words: Transformers for image recognition at scale. *arXiv preprint arXiv:2010.11929*, 2020.

Ruofei Du, Eric Turner, Maksym Dzitsiuk, Luca Prasso, Ivo Duarte, Jason Dourgarian, Joao Afonso, Jose Pascoal, Josh Gladstone, Nuno Cruces, et al. Depthlab: Real-time 3d interaction with depth maps for mobile augmented reality. In *Proceedings of the 33rd Annual ACM Symposium on User Interface Software and Technology*, pp. 829–843, 2020.

David Eigen, Christian Puhrsch, and Rob Fergus. Depth map prediction from a single image using a multi-scale deep network. *Advances in neural information processing systems*, 27, 2014.

Huan Fu, Mingming Gong, Chaohui Wang, Kayhan Batmanghelich, and Dacheng Tao. Deep ordinal regression network for monocular depth estimation. In *Proceedings of the IEEE conference on computer vision and pattern recognition*, pp. 2002–2011, 2018.

Andreas Geiger, Philip Lenz, and Raquel Urtasun. Are we ready for autonomous driving? the kitti vision benchmark suite. In *2012 IEEE conference on computer vision and pattern recognition*, pp. 3354–3361. IEEE, 2012.

Richard Hartley and Andrew Zisserman. *Multiple view geometry in computer vision*. Cambridge university press, 2003.

Kaiming He, Xiangyu Zhang, Shaoqing Ren, and Jian Sun. Deep residual learning for image recognition. In *Proceedings of the IEEE conference on computer vision and pattern recognition*, pp. 770–778, 2016.

Derek Hoiem, Alexei A Efros, and Martial Hebert. Automatic photo pop-up. In *ACM SIGGRAPH 2005 Papers*, pp. 577–584. Association for Computing Machinery, 2005.

Junjie Hu, Mete Ozay, Yan Zhang, and Takayuki Okatani. Revisiting single image depth estimation: Toward higher resolution maps with accurate object boundaries. In *2019 IEEE Winter Conference on Applications of Computer Vision (WACV)*, pp. 1043–1051. IEEE, 2019.

Diederik P Kingma and Jimmy Ba. Adam: A method for stochastic optimization. *arXiv preprint arXiv:1412.6980*, 2014.

Alex Krizhevsky, Ilya Sutskever, and Geoffrey E Hinton. Imagenet classification with deep convolutional neural networks. *Advances in neural information processing systems*, 25, 2012.

Mathieu Labbé and François Michaud. Rtab-map as an open-source lidar and visual simultaneous localization and mapping library for large-scale and long-term online operation. *Journal of Field Robotics*, 36(2):416–446, 2019.

Jin Han Lee, Myung-Kyu Han, Dong Wook Ko, and Il Hong Suh. From big to small: Multi-scale local planar guidance for monocular depth estimation. *arXiv preprint arXiv:1907.10326*, 2019.

Sihaeng Lee, Janghyeon Lee, Byungju Kim, Eojindl Yi, and Junmo Kim. Patch-wise attention network for monocular depth estimation. In *Proceedings of the AAAI Conference on Artificial Intelligence*, volume 35, pp. 1873–1881, 2021.

Bo Li, Chunhua Shen, Yuchao Dai, Anton van den Hengel, and Mingyi He. Depth and surface normal estimation from monocular images using regression on deep features and hierarchical crfs. In *Proceedings of the IEEE Conference on Computer Vision and Pattern Recognition (CVPR)*, June 2015.

Julian Lienen, Eyke Hüllermeier, Ralph Ewerth, and Nils Nommensen. Monocular depth estimation via listwise ranking using the plackett-luce model. In *Proceedings of the IEEE/CVF Conference on Computer Vision and Pattern Recognition (CVPR)*, pp. 14595–14604, June 2021.

Ce Liu, Shuhang Gu, Luc Van Gool, and Radu Timofte. Deep line encoding for monocular 3d object detection and depth prediction. In *32nd British Machine Vision Conference (BMVC 2021)*, pp. 354, 2021a.

Fayao Liu, Chunhua Shen, Guosheng Lin, and Ian Reid. Learning depth from single monocular images using deep convolutional neural fields. *IEEE transactions on pattern analysis and machine intelligence*, 38(10):2024–2039, 2015.

Xingtong Liu, Ayushi Sinha, Masaru Ishii, Gregory D Hager, Austin Reiter, Russell H Taylor, and Mathias Unberath. Dense depth estimation in monocular endoscopy with self-supervised learning methods. *IEEE transactions on medical imaging*, 39(5):1438–1447, 2019.

Ze Liu, Yutong Lin, Yue Cao, Han Hu, Yixuan Wei, Zheng Zhang, Stephen Lin, and Baining Guo. Swin transformer: Hierarchical vision transformer using shifted windows. In *Proceedings of the IEEE/CVF International Conference on Computer Vision*, pp. 10012–10022, 2021b.

Zhuang Liu, Hanzi Mao, Chao-Yuan Wu, Christoph Feichtenhofer, Trevor Darrell, and Saining Xie. A convnet for the 2020s. *arXiv preprint arXiv:2201.03545*, 2022.

Xiaoxiao Long, Cheng Lin, Lingjie Liu, Wei Li, Christian Theobalt, Ruigang Yang, and Wenping Wang. Adaptive surface normal constraint for depth estimation. In *Proceedings of the IEEE/CVF International Conference on Computer Vision*, pp. 12849–12858, 2021.

R Duncan Luce. *Individual choice behavior: A theoretical analysis*. Courier Corporation, 2012.

Ben Mildenhall, Pratul P Srinivasan, Matthew Tancik, Jonathan T Barron, Ravi Ramamoorthi, and Ren Ng. Nerf: Representing scenes as neural radiance fields for view synthesis. *Communications of the ACM*, 65(1):99–106, 2021.

Thomas Mollenhoff, Emanuel Laude, Michael Moeller, Jan Lellmann, and Daniel Cremers. Sublabel-accurate relaxation of nonconvex energies. In *Proceedings of the IEEE Conference on Computer Vision and Pattern Recognition*, pp. 3948–3956, 2016.

Thomas Müller, Alex Evans, Christoph Schied, and Alexander Keller. Instant neural graphics primitives with a multiresolution hash encoding. *arXiv preprint arXiv:2201.05989*, 2022.

Martin R Oswald, Eno Töppe, and Daniel Cremers. Fast and globally optimal single view reconstruction of curved objects. In *2012 IEEE Conference on Computer Vision and Pattern Recognition*, pp. 534–541. IEEE, 2012.

Adam Paszke, Sam Gross, Francisco Massa, Adam Lerer, James Bradbury, Gregory Chanan, Trevor Killeen, Zeming Lin, Natalia Gimelshein, Luca Antiga, et al. Pytorch: An imperative style, high-performance deep learning library. *Advances in neural information processing systems*, 32, 2019.

Vaishakh Patil, Christos Sakaridis, Alexander Liniger, and Luc Van Gool. P3depth: Monocular depth estimation with a piecewise planarity prior. *arXiv preprint arXiv:2204.02091*, 2022.

Xiaojuan Qi, Renjie Liao, Zhengzhe Liu, Raquel Urtasun, and Jiaya Jia. Geonet: Geometric neural network for joint depth and surface normal estimation. In *Proceedings of the IEEE Conference on Computer Vision and Pattern Recognition*, pp. 283–291, 2018.

Siyuan Qiao, Yukun Zhu, Hartwig Adam, Alan Yuille, and Liang-Chieh Chen. Vip-deeplab: Learning visual perception with depth-aware video panoptic segmentation. In *Proceedings of the IEEE/CVF Conference on Computer Vision and Pattern Recognition*, pp. 3997–4008, 2021.

René Ranftl, Katrin Lasinger, David Hafner, Konrad Schindler, and Vladlen Koltun. Towards robust monocular depth estimation: Mixing datasets for zero-shot cross-dataset transfer. *IEEE Transactions on Pattern Analysis and Machine Intelligence (TPAMI)*, 2020.

René Ranftl, Alexey Bochkovskiy, and Vladlen Koltun. Vision transformers for dense prediction. In *Proceedings of the IEEE/CVF International Conference on Computer Vision*, pp. 12179–12188, 2021.

Ashutosh Saxena, Min Sun, and Andrew Y Ng. Learning 3d scene structure from a single still image. In *2007 IEEE 11th international conference on computer vision*, pp. 1–8. IEEE, 2007.

Ashutosh Saxena, Min Sun, and Andrew Y Ng. Make3d: Learning 3d scene structure from a single still image. *IEEE transactions on pattern analysis and machine intelligence*, 31(5):824–840, 2008.

Nathan Silberman, Derek Hoiem, Pushmeet Kohli, and Rob Fergus. Indoor segmentation and support inference from rgbd images. In *European conference on computer vision*, pp. 746–760. Springer, 2012.

Karen Simonyan and Andrew Zisserman. Very deep convolutional networks for large-scale image recognition. *arXiv preprint arXiv:1409.1556*, 2014.

Shuran Song, Samuel P Lichtenberg, and Jianxiong Xiao. Sun rgb-d: A rgb-d scene understanding benchmark suite. In *Proceedings of the IEEE conference on computer vision and pattern recognition*, pp. 567–576, 2015.

Keisuke Tateno, Federico Tombari, Iro Laina, and Nassir Navab. Cnn-slam: Real-time dense monocular slam with learned depth prediction. In *Proceedings of the IEEE conference on computer vision and pattern recognition*, pp. 6243–6252, 2017.

Zachary Teed and Jia Deng. Droid-slam: Deep visual slam for monocular, stereo, and rgb-d cameras. *Advances in Neural Information Processing Systems*, 34:16558–16569, 2021.

Fangjinhua Wang, Silvano Galliani, Christoph Vogel, Pablo Speciale, and Marc Pollefeys. Patchmatchnet: Learned multi-view patchmatch stereo. In *Proceedings of the IEEE/CVF Conference on Computer Vision and Pattern Recognition*, pp. 14194–14203, 2021.

Ke Xian, Jianming Zhang, Oliver Wang, Long Mai, Zhe Lin, and Zhiguo Cao. Structure-guided ranking loss for single image depth prediction. In *Proceedings of the IEEE/CVF Conference on Computer Vision and Pattern Recognition*, pp. 611–620, 2020.

Guanglei Yang, Hao Tang, Mingli Ding, Nicu Sebe, and Elisa Ricci. Transformer-based attention networks for continuous pixel-wise prediction. In *Proceedings of the IEEE/CVF International Conference on Computer Vision*, pp. 16269–16279, 2021.

Wei Yin, Yifan Liu, Chunhua Shen, and Youliang Yan. Enforcing geometric constraints of virtual normal for depth prediction. In *Proceedings of the IEEE/CVF International Conference on Computer Vision*, pp. 5684–5693, 2019.

Weihao Yuan, Xiaodong Gu, Zuozhuo Dai, Siyu Zhu, and Ping Tan. New crfs: Neural window fully-connected crfs for monocular depth estimation. *arXiv e-prints*, pp. arXiv–2203, 2022.

Daniel Zoran, Phillip Isola, Dilip Krishnan, and William T Freeman. Learning ordinal relationships for mid-level vision. In *Proceedings of the IEEE international conference on computer vision*, pp. 388–396, 2015.

A APPENDIX

A.1 TRAINING DETAILS

We implement our framework in PyTorch (Paszke et al., 2019). We adopt the Swin-Large (Liu et al., 2021b) as our backbone to conduct ablation experiments and compare with the state-of-the-arts. And the backbone is pre-trained on ImageNet-22K (Deng et al., 2009) by image classification. For training, we use the Adam optimizer (Kingma & Ba, 2014) without weight decay. We decrease the learning rate from 3e-5 to 1e-5 by the cosine annealing scheduler. To avoid over-fitting, we augment the images by horizontal flipping. For both training and test, we keep the resolution of images to be 352×1216 in KITTI (Geiger et al., 2012), and 480×640 in both NYU Depth V2 (Silberman et al., 2012) and SUN RGB-D (Song et al., 2015). In KITTI, the model is trained for 10 epochs for the official split and 20 epochs for the Eigen split (Eigen et al., 2014). In NYU Depth V2, the model is trained for 20 epochs. We set the batch size to be 4 and 8 respectively for ablation experiments and comparison with the state-of-the-art.

A.2 EVALUATION METRICS

Supposing the predicted and ground-truth depth to be $\hat{Z} \in \mathbb{R}^{m \times n}$ and $Z_{gt} \in \mathbb{R}^{m \times n}$, respectively, and the number of valid pixels to be N. We follow the existing methods (Yuan et al., 2022) and utilize the following measures for quantitative evaluation:

- square root of the Scale Invariant Logarithmic error (**SILog**): $\frac{1}{N}\sum_{i,j}(e^{i,j})^2 - \frac{1}{N^2}(\sum_{i,j} e^{i,j})^2$, where $e^{i,j} = \log \hat{Z}^{i,j} - \log Z_{gt}^{i,j}$;
- Relative Squared error (**Sq Rel**): $\frac{1}{N}\sum_{i,j}(\hat{Z}^{i,j} - Z_{gt}^{i,j})^2 / Z_{gt}^{i,j}$;
- Relative Absolute Error (**Abs Rel**): $\frac{1}{N}\sum_{i,j}|\hat{Z}^{i,j} - Z_{gt}^{i,j}| / Z_{gt}^{i,j}$;
- Root Mean Squared error (**RMS**): $\frac{1}{N}\sqrt{\sum_{i,j}(\hat{Z}^{i,j} - Z_{gt}^{i,j})^2}$;
- Root Mean Squared Logarithmic error (**RMS log**): $\frac{1}{N}\sqrt{\sum_{i,j}(e^{i,j})^2}$;
- threshold accuracy ($\boldsymbol{\delta_k}$): percentage of $\hat{Z}^{i,j}$ s.t. $\max(\frac{\hat{Z}^{i,j}}{Z_{gt}^{i,j}}, \frac{Z_{gt}^{i,j}}{\hat{Z}^{i,j}}) < 1.25^k$.

A.3 DERIVATION OF THE VARIATIONAL CONSTRAINT

In this part, we introduce the derivation of the variational constraint in more detail. Firstly, we present the specific form of the difference operator P, the confidence weight matrix $\tilde{\Sigma}$, the difference vector $\tilde{\Gamma}$ and the depth vector $\tilde{Z}_u$, when the depth map Z_u is at resolution 2×2. Secondly we show the derivation of the optimal solution $\tilde{Z}_u^*$.

Overall Matrix Form Suppose the unscaled depth map to be $Z_u \in \mathbb{R}^{2\times 2}$, the difference map to be $\Gamma_x \in \mathbb{R}^{2\times 2}$ and $\Gamma_y \in \mathbb{R}^{2\times 2}$, and the corresponding confidence weight to be $\Sigma_x \in [0,1]^{2\times 2}$ and $\Sigma_y \in [0,1]^{2\times 2}$. We first reorganize the elements in $\Gamma_x, \Gamma_y, \Sigma_x, \Sigma_y$ to construct the difference vector $\tilde{\Gamma} \in \mathbb{R}^{8\times 1}$ and the confidence weight matrix $\tilde{\Sigma} \in \mathbb{R}^{8\times 8}$:

$$\tilde{\Gamma} = \begin{pmatrix} \Gamma_x^{1,1} \\ \Gamma_x^{1,2} \\ \Gamma_x^{2,1} \\ \Gamma_x^{2,2} \\ \Gamma_y^{1,1} \\ \Gamma_y^{1,2} \\ \Gamma_y^{2,1} \\ \Gamma_y^{2,2} \end{pmatrix}, \tilde{\Sigma} = \begin{pmatrix} \Sigma_x^{1,1} & 0 & 0 & 0 & 0 & 0 & 0 & 0 \\ 0 & \Sigma_x^{1,2} & 0 & 0 & 0 & 0 & 0 & 0 \\ 0 & 0 & \Sigma_x^{2,1} & 0 & 0 & 0 & 0 & 0 \\ 0 & 0 & 0 & \Sigma_x^{2,2} & 0 & 0 & 0 & 0 \\ 0 & 0 & 0 & 0 & \Sigma_y^{1,1} & 0 & 0 & 0 \\ 0 & 0 & 0 & 0 & 0 & \Sigma_y^{1,2} & 0 & 0 \\ 0 & 0 & 0 & 0 & 0 & 0 & \Sigma_y^{2,1} & 0 \\ 0 & 0 & 0 & 0 & 0 & 0 & 0 & \Sigma_y^{2,2} \end{pmatrix}.$$

Next, we apply the difference operator $P \in \mathbb{R}^{8\times 4}$:

$$P = \begin{pmatrix} -1 & 1 & 0 & 0 \\ 0 & -1 & 1 & 0 \\ 0 & 0 & -1 & 1 \\ 0 & 0 & 0 & 0 \\ -1 & 0 & 1 & 0 \\ 0 & -1 & 0 & 1 \\ 0 & 0 & 0 & 0 \\ 0 & 0 & 0 & 0 \end{pmatrix}$$

on the depth vector $\tilde{Z}_u \in \mathbb{R}^{4\times 1}$:

$$\tilde{Z}_u = \begin{pmatrix} Z_u^{1,1} \\ Z_u^{1,2} \\ Z_u^{2,1} \\ Z_u^{2,2} \end{pmatrix}.$$

Finally, we construct the following constraint equation:

$$\tilde{\Sigma} P \tilde{Z}_u = \tilde{\Sigma}\tilde{\Gamma}. \tag{9}$$

In the above equation, each row represents a weighted constraint for the first-order difference along the x-axis:

$$\Sigma_x^{i,j}(Z_u^{i,j+1} - Z_u^{i,j}) = \Sigma_x^{i,j}\Gamma_x^{i,j} \tag{10}$$

or along the y-axis:

$$\Sigma_y^{i,j}(Z_u^{i+1,j} - Z_u^{i,j}) = \Sigma_y^{i,j}\Gamma_y^{i,j} \tag{11}$$

where $(Z_u^{i,j+1} - Z_u^{i,j}) = \Gamma_x^{i,j}$ and $(Z_u^{i+1,j} - Z_u^{i,j}) = \Gamma_y^{i,j}$ are the variational constraints for the first-order difference, while $\Sigma_x^{i,j}$ and $\Sigma_y^{i,j}$ are the confidence weights for the constraints.

Optimal Solution Given $\tilde{\Sigma}$ and $\tilde{\Gamma}$, we search for the optimal depth vector $\tilde{Z}_u^*$ by minimizing the residual of Eq.(9):

$$\tilde{Z}_u^* = \arg\min_{\tilde{Z}_u} ||\tilde{\Sigma}(P\tilde{Z}_u - \tilde{\Gamma})||_2. \tag{12}$$

Firstly, the objective function, $||\tilde{\Sigma}(P\tilde{Z}_u - \tilde{\Gamma})||_2$, is convex with respect to $\tilde{Z}_u$. Because $||\cdot||_2$ is a convex function. A composition of $||\cdot||_2$ and affine function , $\tilde{\Sigma}(P\tilde{Z}_u - \tilde{\Gamma})$, is still convex.

Secondly, the optimal solution of a convex function can be found at where the first derivative is zero. Thereby we obtain the final solution $\tilde{Z}_u^* = (P^T\tilde{\Sigma}^2 P)^{-1}P^T\tilde{\Sigma}^2\tilde{\Gamma}$.

A.4 Ablation on KITTI and SUN RGB-D

To further demonstrate the benefits of our V-layer on KITTI Eigen split (Geiger et al., 2012; Eigen et al., 2014) and SUN RGB-D test set (Song et al., 2015), we present the performance of the predicted depth map when replacing the V-layer with a single convolutional layer. As shown in Tab.(9), our V-layer can improve the depth map accuracy on both KITTI and SUN RGB-D.

Table 9: **Benefit of V-layer.** We replace the proposed V-layer with a single convolutional layer, and evaluate the predicted depth map accuracy.

Dataset	Layer	SILog ↓	Abs Rel ↓	RMS↓	RMS log↓	δ_1 ↑	δ_2 ↑
KITTI	Convolution	6.996	0.052	0.217	0.079	0.975	**0.997**
	V-Layer	**6.817**	**0.050**	**0.209**	**0.076**	**0.977**	**0.997**
SUN	Convolution	13.172	0.098	0.309	0.132	0.924	0.981
	V-Layer	**12.596**	**0.094**	**0.299**	**0.127**	**0.929**	**0.983**

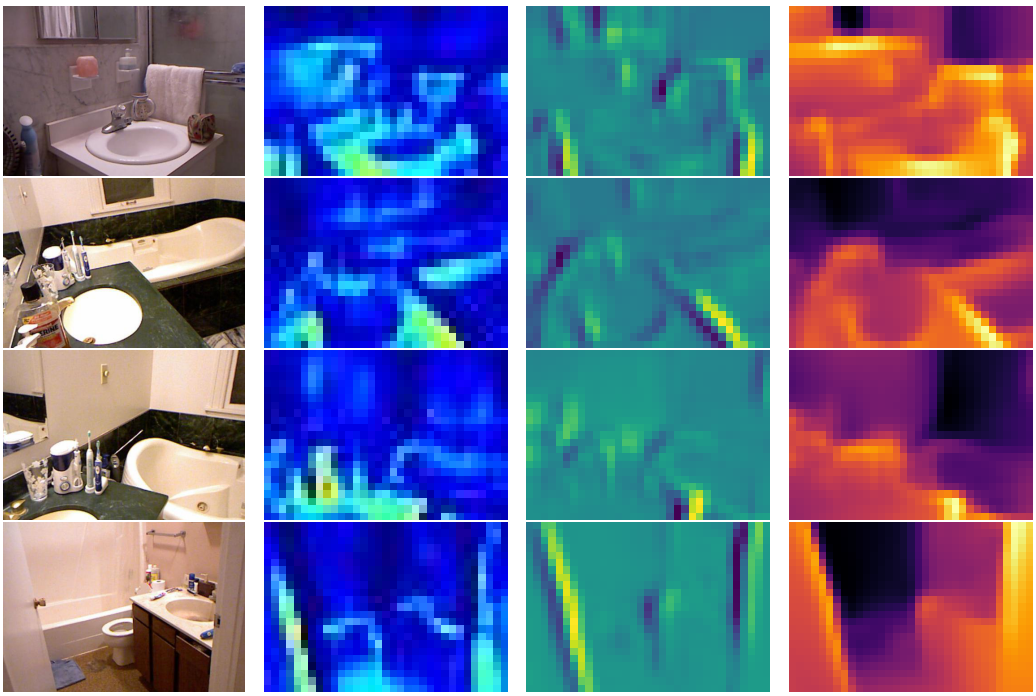

(a) Image (b) Confidence Weight (c) Difference Map (d) Depth Map

Figure 6: **Visualization of V-layer Prediction.** We visualize the confidence weight Σ_x, the difference map Γ_x and the depth map Z_u from the V-layer when predicting on NYU Depth V2 test set.

A.5 More Visualization

We visualize the confidence weight Σ_x, the difference map Γ_x, and the depth map Z_u from the V-layer in Fig.6. We observe that the depth value of a pixel shows correlation with respect to the image coordinates of the pixel. For example, in the last example in Fig.6, for different pixels at the door, the depth values are usually different but the first order difference are approximately the same. This observation shows that the difference map might be easier to predict than the depth map.

A.6 Qualitative Results

We provide more qualitative results on KITTI Eigen split (Eigen et al., 2014), SUN RGB-D (Song et al., 2015), and NYU Depth V2 (Silberman et al., 2012) in Fig.7, Fig.8 and Fig.9, respectively. Our framework can predict more accurate shapes and preserve the high-frequency scene details.

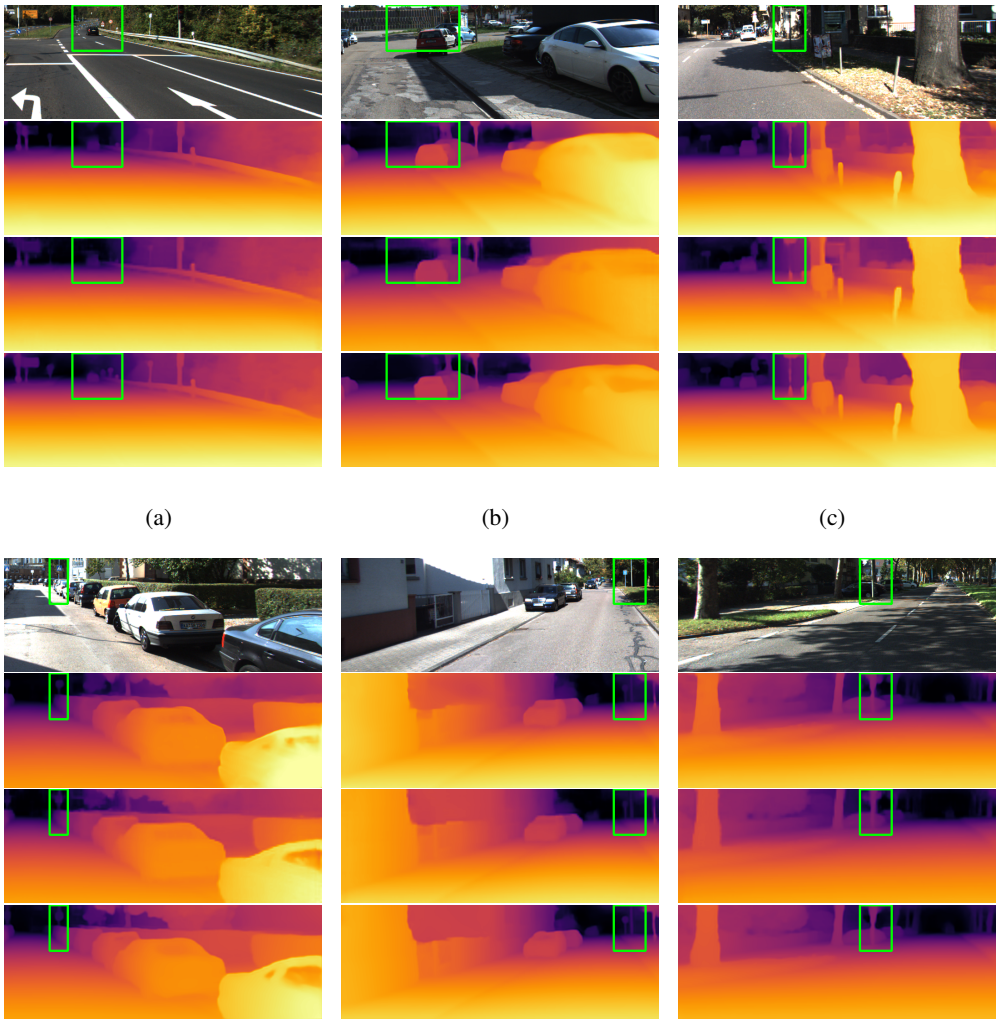

Figure 7: Qualitative comparison on KITTI Eigen split (Eigen et al., 2014). For each column, from top to bottom we present the input image, the prediction from AdaBins (Bhat et al., 2021), NeWCRFs (Yuan et al., 2022), and our framework respectively.

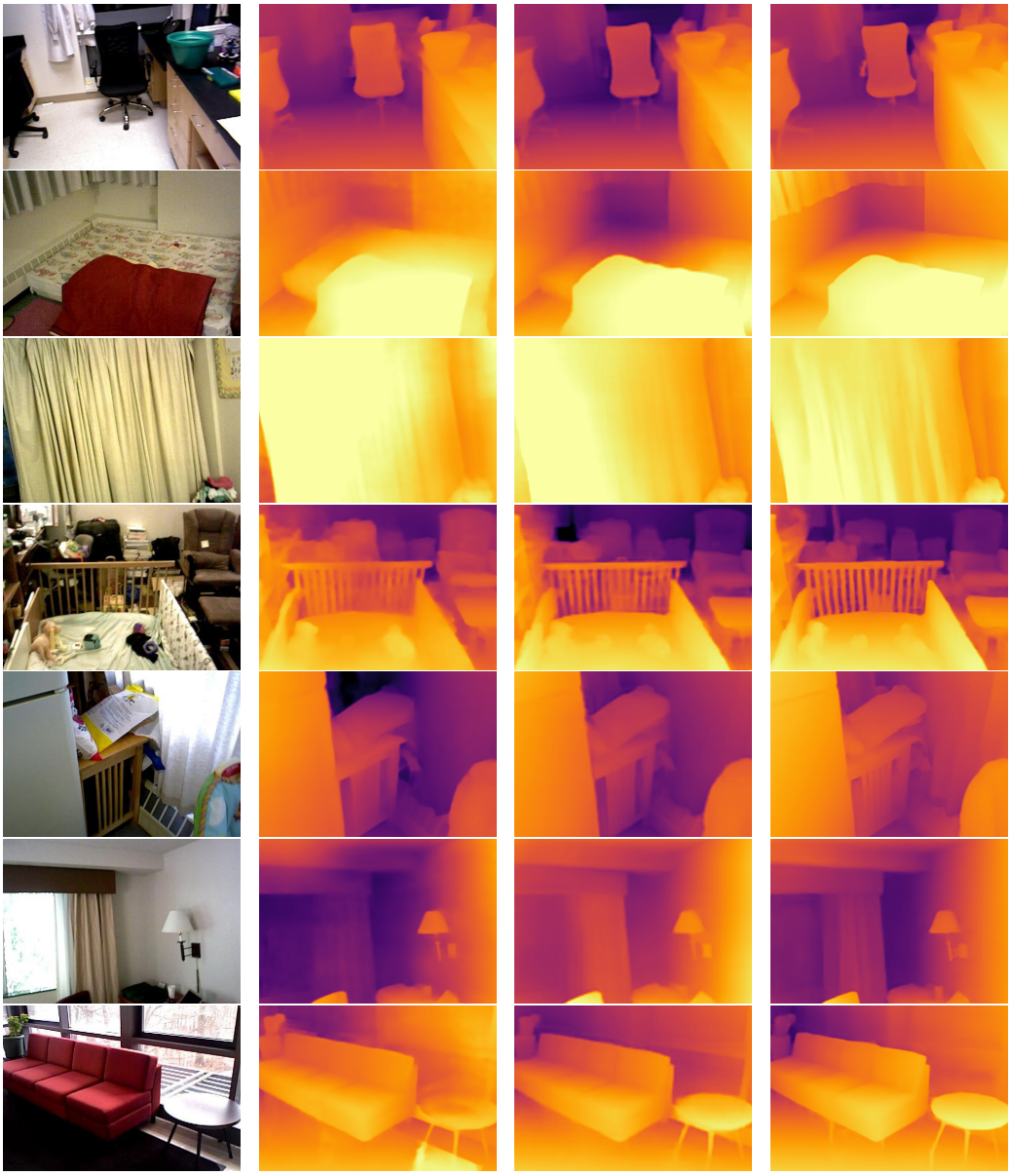

(a) Image (b) AdaBins (c) NeWCRFs (d) Ours

Figure 8: Qualitative comparison with AdaBins (Bhat et al., 2021), NeWCRFs (Yuan et al., 2022) on SUN RGB-D test set (Song et al., 2015). All the models are pre-trained on NYU Depth V2 (Silberman et al., 2012) training set.

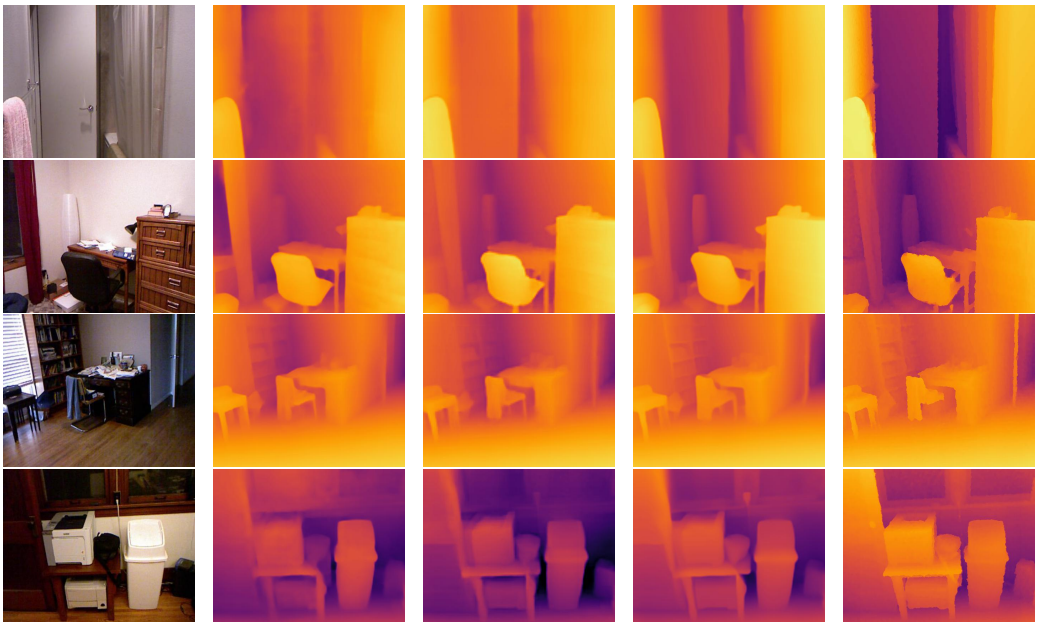

(a) Image (b) AdaBins (c) NeWCRFs (d) Ours (e) Ground Truth

Figure 9: Qualitative comparison with AdaBins (Bhat et al., 2021), NeWCRFs (Yuan et al., 2022) on NYU Depth V2 test set (Silberman et al., 2012). The ground-truth depth map are in-painted for visualization.